Energy Storage Materials 91 (2026) 105551

Contents lists available at ScienceDirect

Energy Storage Materials

journal homepage: www.elsevier.com/locate/ensm

Cellulose swelling chemistry enables biomass-derived hard carbons with high-rate plateau capability for sodium ion batteries

Kai Gu [1,a], Junan Feng [1,a], Taiping Zeng [a], Jingye Wang [a], Guilin Feng [a], Wen Xi [a], Yihan Wang [b], Jiahao Chen [a], Minjie Chen [a], Feitian Ran [d], Jifei Liu [d], Chunliu Xu [a,b,*], Yao Xiao [c,*], Weiqing Yang [a,b,*]

[a] Key Laboratory of Advanced Technologies of Materials (Ministry of Education), School of Materials Science and Engineering, Southwest Jiaotong University, Chengdu, 610031, China
[b] Research Institute of Frontier Science, Southwest Jiaotong University, Chengdu, 610031, China
[c] College of Chemistry and Materials Engineering, Wenzhou University, Wenzhou, Zhejiang, 325035, China
[d] School of New Energy and Power Engineering, Lanzhou Jiaotong University, Lanzhou, Gansu, 730070, China

ARTICLE INFO

Keywords:
Biomass-derived hard carbon
Sodium-ion batteries
Cellulose swelling
Closed pores
High-rate performance

ABSTRACT

Cellulose-rich biomass combines low cost, natural abundance and flexible microstructural tunability, thereby positioning itself as one of the most attractive precursors for fabricating high-performance hard carbons (HCs) anodes used in sodium-ion batteries (SIBs). However, constructing closed-pore structures within the robust macromolecular cellulose of biomass remains challenging for extending the plateau capacity and enhancing the diffusion kinetics of HCs. Herein, we propose an innovative swelling pretreatment strategy for cellulose using lithium hydroxide (LiOH) as the swelling reagent. Molecular dynamics simulations reveal that hydrated lithium ions penetrate the crystalline regions of cellulose and remain trapped during low-temperature drying, subsequently generating steam vapor upon carbonization to create closed pores. As a proof of concept, after swelling treatment with a moderate LiOH solution, the optimized ramie-derived HCs enables a superior rate capability of 195.7 mAh g^{-1} at an ultra-high rate of 6,000 mA g^{-1}. Combined in-/ex-situ characterization and GITT analysis delineate a three-stage sodium ions diffusion/storage process in HCs, uncovering the competitive kinetics between side reactions and the closed-pore dominated sodium cluster formation mechanism, which provides crucial insight for optimizing high-rate performance in SIBs. Overall, this study advances the mechanistic understanding of high-rate sodium storage and presents a novel material design strategy, offering valuable guidance for the development of next-generation biomass-derived anode materials for SIBs.

1. Introduction

Compared with lithium-ion batteries (LIBs), sodium-ion batteries (SIBs) have more abundant resources and more reliable safety performance, such as lower dendrite growth probability and higher thermal runaway temperature, which makes SIBs become one of the most promising candidates for LIBs [1–4]. Due to the comprehensive consideration of production cost and process simplicity, as well as the goal of all mankind to implement the concept of green and sustainable development, biomass and its waste as the precursor of hard carbons (HCs) in SIBs anodes is of vital strategic significance [5,6]. Up to so far, a variety of biomass-derived HCs have been verified to exhibit good performance in SIBs, including coconut shell, bamboo powder, reed rod, and starches, et al [7–16]. Ramie, an annual triple-harvest shrub primarily grown in Dazhu, Sichuan, has a national planting area of about 28,100 hectares with an average annual output of 53,000 tons of raw hemp, contributing to lower costs and greater economic benefits. Additionally, the high cellulose content and natural pore-structures of ramie provide a solid foundation for the preparation of high-performance energy storage carbon materials. Our previous studies have demonstrated that ramie-derived porous carbon has huge application values in supercapacitors, which inspired us to further explore its application possibilities for SIBs [17–23]. Despite extensive research, HCs materials derived from biomass precursors still suffer from

* Corresponding authors.
E-mail addresses: chunliuxu@swjtu.edu.cn (C. Xu), xiaoyao@wzu.edu.cn (Y. Xiao), wqyang@swjtu.edu.cn (W. Yang).
[1] These authors contributed equally to this work.

https://doi.org/10.1016/j.ensm.2026.105551
Received 28 July 2026; Received in revised form 31 August 2026; Accepted 20 September 2026
Available online 21 September 2026
2405-8297/© 2026 Elsevier B.V. All rights are reserved, including those for text and data mining, AI training, and similar technologies.

unreliable electrochemical performance, typically characterized by high slope capacity and low plateau capacity at high rates, which severely restricts the output voltage and power density of full-cells, thereby hindering their practical application [24–26]. It is widely recognized that constructing a well-developed closed pore structure is the key to achieving HCs anodes with long low-voltage plateau regions [27]. However, the currently reported methods for creating closed pores, such as alkali treatment, activation and templating, usually involve complex procedures and are tedious to implement, or are only effective for specific biomass feedstocks [28–30]. In this context, there is an urgent need to develop a green, efficient, and simple strategy that can precisely engineer closed pores at the molecular level of cellulose. As is well known, cellulose is a linear long-chain polysaccharide composed of D-pyranoglucosyl units connected by β-1,4 glycosidic bonds, and the long chains are interconnected through hydrogen bonds (HBs). This arrangement creates highly ordered crystalline regions alongside relatively disordered amorphous regions. Cellulose swelling describes physicochemical transformation involving the partial relaxation of cellulose structures upon interaction with polar solvent molecules, and the process is categorized into inter-crystalline and intra-crystalline swelling, depending on whether polar molecules penetrate the crystalline regions [31]. Generally, polar molecules, such as water (H_2O) molecules, can only access the loosely packed amorphous regions, leading to inter-crystalline swelling. And these H_2O molecules in the amorphous regions can be easily removed by a simple drying process. In contrast, previous studies have demonstrated that alkali solutions (e.g., LiOH) are good swelling agents for cellulose, and metal ions in alkaline solutions usually exist in the form of hydrated ions ($Li[(H_2O)_n]^+$), which can break HBs and penetrate the crystalline region of cellulose, resulting in intra-crystalline swelling [32]. Since the alkali metal ions with smaller radii have stronger adsorption forces on surrounding H_2O molecules, which can form larger-diameter hydrated ions, favorably entering crystalline regions of cellulose. Therefore, the swelling ability of several alkalis' solution is at the order of LiOH > NaOH > KOH > RbOH > CsOH [33].

Herein, this study utilized the cellulose swelling strategy, combined with appropriate carbonization temperature conditions, focusing on regulating the closed-pore characteristics of HCs derived from ramie stalks. Specifically, using a large-diameter and highly polar hydrated ion obtained from LiOH hydrolysis disrupted the hydroxyl groups (−OH) in the crystalline regions, thereby inducing irreversible expansion and leaving some pore cavities. During the subsequent pyrolysis process, accompanied by carbon layer rearrangement, these pore cavities were transformed into closed pores. As a validation, two key mechanisms were explained using molecular dynamics simulation, namely that $Li[(H_2O)_n]^+$ truly enters the interlayers of the cellulose crystalline region, triggering intra-crystalline swelling, and the H_2O molecular in the crystalline region does not escape during the drying process at 110°C. As the carbonization temperature increased, the physical parameters and surface oxygen functional group properties of the samples changed significantly. Among them, the optimized ramie-derived HCs exhibited a combination of high closed-pore content and the highest carbonyl (C=O) proportion which has been widely confirmed to enhance the electrochemical performance of HCs. Remarkably, the optimized anodes demonstrated a high reversible capacity of 322.33 mAh g^{-1} at 30 mA g^{-1} (0.1 C) with an initial Coulombic efficiency (ICE) of 86.11%, and a long cycling life with an 84.54% retention rate after 1,200 cycles at 2 C. Even under the high rate of 20 C, the obtained HCs still maintained a specific capacity of 195.69 mAh g^{-1}. Full-cell tests demonstrated practical applicability, showing a capacity retention rate of 81.09% after 300 cycles at 2 C. Furthermore, in-situ X-ray diffraction and ex-situ Raman spectroscopy revealed the diffusion and storage behavior of sodium ions (Na^+) during the charge/discharge process, combined with galvanostatic intermittent titration technique (GITT) results in explaining the changes of Na^+ diffusion characteristics. This work emphasized the positive role of swelling strategy in inducing closed-pore formation, providing meaningful guidance for the rational design of HCs microstructure, which will benefit the further high-value utilization of waste biomass in the development of high-rate SIBs.

2. Results and discussion

2.1. Concept design of swelling strategy to construct closed pores

Ramie stalks with natural porous structure and high cellulose content were used as the precursor of HCs (Fig. S1). According to different swelling agents, the precursors were respectively defined as water treated ramie (WTR) and cellulose swelling ramie (CSR), respectively. After carbonization at 1200°C, the resulting HCs were designated as CSHC1200 (from CSR) and WTHC1200 (from WTR). The structure variation details of the cellulose swelling, drying and carbonization process were schematically described in Fig. 1.

For CSR, when cellulose was exposed to LiOH solution, $Li[(H_2O)_n]^+$ infiltrated the amorphous regions and made the molecular chains gradually unfold. Then, $Li[(H_2O)_n]^+$ initiated a reaction with −OH in the crystalline regions, progressively disrupting the HBs between them. Since $Li[(H_2O)_n]^+$ has a diameter of about 0.76 nm, which is larger than the interlayer spacing of cellulose of about 0.39 nm, its insertion causes interlayer expansion, disrupts HBs, gradually fractures the crystalline regions, relaxes the molecular chain structure, and simultaneously induces significant intra-crystalline expansion. During the volume expansion of cellulose, molecular bonds broke and chain segments moved, extruding impurity molecules incompatible with $Li[(H_2O)_n]^+$. As a result, the originally regular arrangement and impurity content gradually diminished, with the amorphous regions expanding. In the subsequent drying process, $Li[(H_2O)_n]^+$ within the crystalline cellulose cannot be removed by the relatively low-temperature dry process (usually < 110°C). Therefore, during the higher-temperature carbonization process, $Li[(H_2O)_n]^+$ gained enough kinetic energy and escaped from the cellulose, generating steam vapor to create pore cavities among cross-linked matrixes, finally leading to generation of closed pores in CSHC1200. For comparison, in WTR, H_2O molecules can only reach the amorphous regions, leading to inter-crystalline swelling. However, these H_2O molecules are prone to escape during the drying process. Finally, the rigid cellulose crystals formed more-ordered structures but with fewer closed pores after high-temperature pyrolysis (WTHC1200).

2.2. Theoretical calculation and experimental verification

Based on the above analysis of the mechanisms of structural evolution during cellulose swelling, drying, and carbonization, we used molecular dynamics (MD) simulations to theoretically verify two key scientific questions at the atomic scale: (i) whether $Li[(H_2O)_n]^+$ can truly enter the interlayer of cellulose crystalline region, triggering intra-crystalline swelling; (ii) whether H_2O in the crystalline region will escape during the drying process at 110°C. Firstly, a quantitative comparative analysis of the structural evolution of cellulose in H_2O and LiOH systems was conducted, to elucidate the microscopic physicochemical mechanisms underlying LiOH-induced cellulose swelling at the molecular level (Fig. S2). In terms of macroscopic volume evolution, both systems rapidly reached an equilibrium state following relaxation. Compared with H_2O system, the cellulose structure in LiOH system exhibits a significantly larger equilibrium volume (Fig. 2a), which intuitively confirms that LiOH can induce a more pronounced volumetric expansion effect. To investigate the origin of this macroscopic expansion, we further calculated the normalized gyration radius ($R_g(t)/R_g(0)$) of the cellulose polymer chains. As shown in Fig. 2b, the $R_g(t)/R_g(0)$ value fluctuates mainly around 1.0 in H_2O system, indicating that the cellulose chains maintain a relatively compact and rigid conformation. In contrast, in the LiOH system, the $R_g(t)/R_g(0)$ value increases significantly over time and stabilizes at ~1.05. The increase in $R_g(t)/R_g(0)$ signifies a marked uncoiling and conformational unfolding of the long

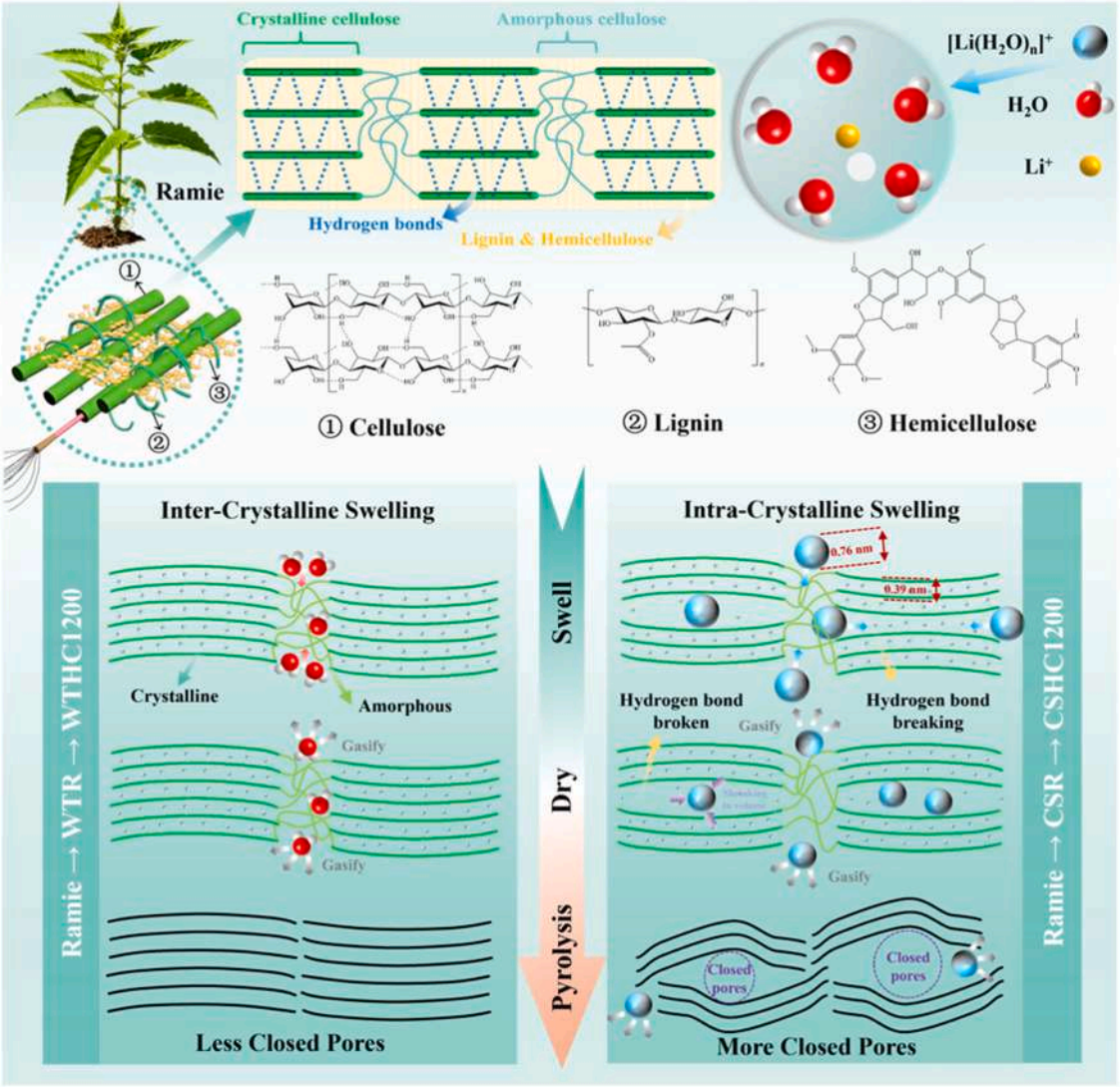


Fig. 1. Schematic illustration of LiOH-swelling inducing the formation of closed pores in the crystalline regions of cellulose. The upper part shows a schematic diagram of the ramie plant and its microscopic structure, with the main components being cellulose, lignin, and hemicellulose. The bottom illustrates the mechanism of closed-pore formation induced by the swelling process.

cellulose chains, which is a typical mesoscopic feature of deep polymer swelling. The fundamental cause of this mesoscale chain segment unfolding lies in the restructuring and disruption of the HBs network. We conducted continuous tracking of the number of intra-molecular and inter-molecular HBs within the system. As shown in Fig. 2c and Fig. S3, H_2O can only penetrate the loosely packed amorphous regions in H_2O system, leading to inter-crystalline swelling; consequently, the system maintains a high number of inter-molecular (~1300) and intra-molecular (~300) HBs, indicating the orderliness of crystalline regions and the rigidity of individual chains. Upon the introduction of LiOH, the highly polar $Li[(H_2O)_n]^+$ effectively disrupts HBs and penetrates the crystalline regions of cellulose, leading to intra-crystalline swelling. This is manifested by a significant reduction in the number of intermolecular HBs responsible for anchoring adjacent cellulose chains to ~1100, whilst the number of intramolecular HBs determining single-chain rigidity drops sharply to ~150. The aforementioned MD simulations demonstrate the strong solvating effect of $Li[(H_2O)_n]^+$, which disrupts the double HBs network within cellulose, increasing the degrees of freedom of the cellulose chains at a microscopic scale and ultimately leading to significant swelling at a macroscopic scale.

Additionally, we conducted MD simulations to verify the mechanisms by which the swelling strategy imparts excellent hydro-locking performance to the crystalline regions (Fig. S4). Firstly, to visually assess the volatility kinetics of the systems, we counted the cumulative number of escaping H_2O molecules that crossed the gas-solid interface within 1 ns at 110°C (Fig. 2d). The H_2O system exhibited a continuous and high-frequency stepwise increase, indicating that H_2O molecules continuously diffuse toward the interface and desorb. In contrast, the evaporation flux of LiOH system was significantly suppressed. Although a small amount of surface free H_2O was removed at the early stage of the simulation (< 100 ps), a kinetic stagnation lasting up to 400 ps appeared in the 480–880 ps interval. This directly confirmed at the macroscopic kinetic level that the system can lock most of the H_2O molecules inside the cellulose at 110°C, laying the prerequisite for subsequent high-temperature carbonization and closed-pores formation. The huge difference in interfacial evaporation behavior originates from changes in the microscopic mobility of H_2O molecules. As shown by the mean square displacement (MSD) curves in Fig. 2e, H_2O molecules in the H_2O system exhibit typical free diffusion characteristics, with MSD increasing linearly over time with a steep slope. In contrast, the diffusive capability of H_2O molecules in the LiOH system drops dramatically, and the MSD is strongly suppressed, indicating that the translational degrees of freedom of H_2O molecules are reduced and in a confined state. We further calculated the radial distribution function (RDF) between Li^+

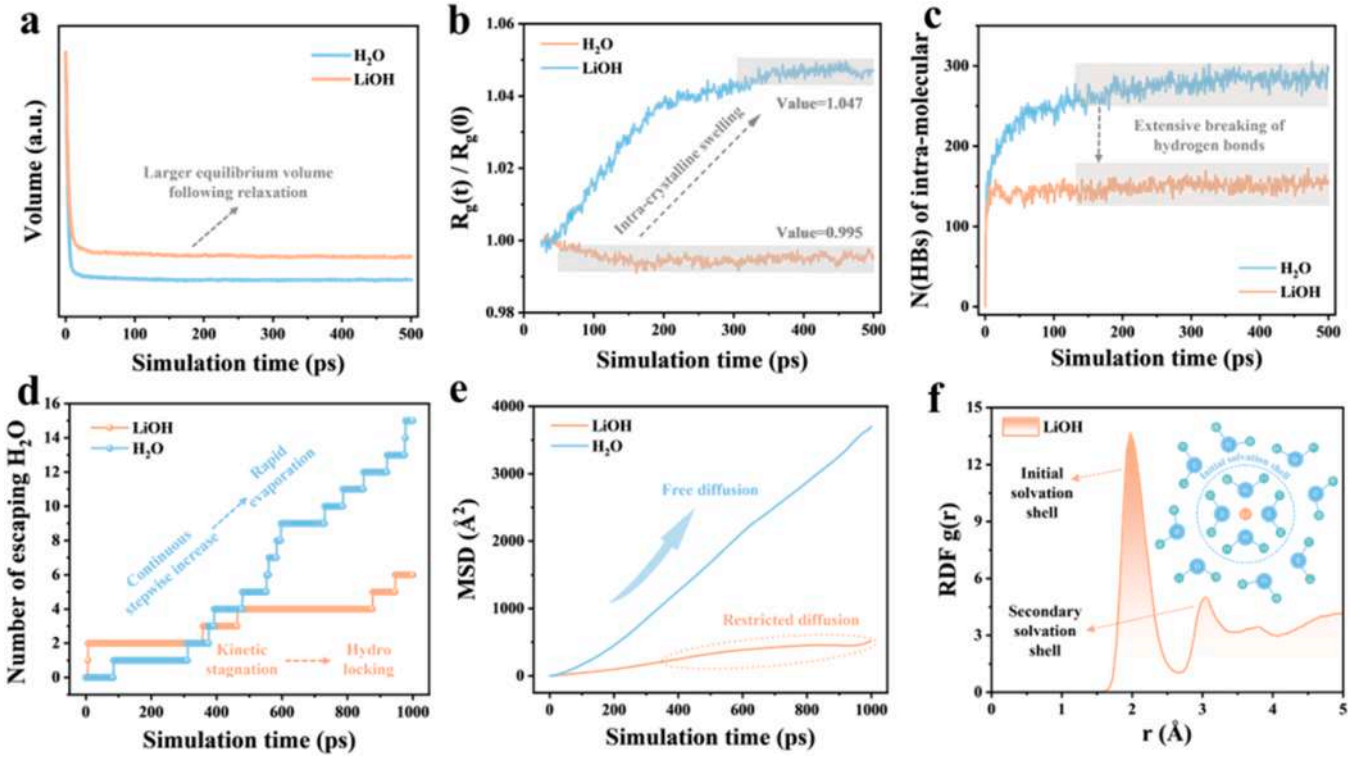


Fig. 2. Molecular dynamics (MD) simulation results based on Lammps on the swelling and drying processes of cellulose in the H_2O and LiOH systems. (a) Evolution of macroscopic volume; (b) normalized turning radius ($R_g(t)/R_g(0)$); (c) number of intra-molecular hydrogen bonds (HBs) in single cellulose polymer long chains during swelling process. (d) The cumulative number of H_2O molecules escaping across the gas-solid interface within 1 ns at 110°C; (e) mean squared displacement (MSD) curve; and (f) radial distribution function (RDF) of Li^+ with H_2O molecules (O atoms) during drying process.

and H_2O molecules (O atoms) to reveal the fundamental thermodynamic origin of the above confinement effect (Fig. 2f). The curve shows an extremely sharp and isolated strong coordination peak at r ≈ 1.95 Å, corresponding to the highly stable primary solvation shell formed by Li and H_2O molecules. In addition, a secondary peak at r ≈ 3 Å indicates that strong ion-dipole interactions further polarize the secondary solvation shell H_2O molecules. This strong Li−O ion coordination locks free H_2O, forming bulky and massive $Li[(H_2O)_n]^+$, reducing the activity of H_2O molecules. Consequently, this kinetically leads to the stagnation of H_2O molecular diffusion, ultimately reducing the vaporization of H_2O molecules.

To elucidate the intra-crystalline swelling of cellulose in CSR at the molecular level, a series of spectra analysis was conducted. X-ray diffraction (XRD) pattern demonstrates the successful conversion of cellulose I to cellulose II in the swollen ramie precursor, accompanied by a shift of the (002) diffraction peak toward lower angles (Fig. 3a). This shift indicates an expansion of the interlayer spacing within cellulose crystalline regions, resulting from the intercalation of $Li[(H_2O)_n]^+$. Besides, the marked attenuation of –OH stretching band near 3440 cm^{-1} in Fourier transform infrared spectroscopy (FT-IR) spectrum provides strong evidence for the disruption of the hydrogen-bonding network within the crystalline regions by $Li[(H_2O)_n]^+$ (Fig. S5). X-ray photoelectron spectroscopy (XPS) results reveal significant changes in the elemental composition after treatment (Table S1). The Li content reaches 2.38 at.% in CSR, confirming the effective incorporation of Li^+ into crystalline regions (Fig. S6a). Notably, the impurity Si content decreases from 3.64 at.% in WTR to 0.68 at.% in CSR, which can be attributed to the removal of impurities during the swelling-induced cleavage and rearrangement of cellulose chains. This purification effect is beneficial for the subsequent performance of the samples. Deconvolution of the high-resolution O 1s spectrum resolves three contributions (Fig. S6b), assigned to C=O (~533.6 eV), –OH (~532.5 eV), and C–O/C–O–Li^+ (~531.3 eV). The relative decrease in –OH component alongside the increase in C–O/C–O–Li^+ fraction aligns with the expected reaction pathway, wherein a –OH is deprotonated and coordinate with Li^+ to form a C–O–Li^+ structure. Collectively, these structural and chemical characterizations provide a coherent and robust validation of the proposed swelling mechanism. Then CSHC1200 and WTHC1200 were subjected to comprehensive characterization measurement. Scanning electron microscope (SEM) images revealed that both samples maintained good morphology inheritance from ramie stalks, preserving natural porous architectures (Fig. 3b and Fig. S7). In addition, from the inset of Fig. 3b, the darker color of CSR compared to WTR also provides visual evidence of its cellulose swelling process. This color change primarily stems from the disruption of the dense structure in ramie stalks, which exposes internal chromophores (e.g., lignin) and enhances the oxidation propensity of oxygen-containing functional groups (OCFGs) on the cellulose chains. Notably, the edges of CSHC1200 particles exhibited a distinct delaminated architecture, whereas WTHC1200 appears as an integrated aggregate without slice, directly reflecting the microstructural impact of swelling. High-resolution transmission electron microscopy (HR-TEM) was conducted for further characterization. As presented in Fig. 3c, WTHC1200 displayed a prevalent long-range ordered graphitic carbon layer structure originating from cellulose, which was absent in CSHC1200. The distinction can be attributed to swelling process, where the physicochemical interaction of large-diameter $Li[(H_2O)_n]^+$ with the cellulose crystalline regions effectively disrupted the original ordered structure. As shown in Fig. 3d, both materials displayed two broadened characteristic peaks at approximately 24° and 43° in XRD spectra, corresponding to (002) and (100) crystal planes of graphite respectively, indicative of an amorphous structure. It is noteworthy that the (002) peak shifted to a lower angle after swelling, a phenomenon attributed to the spatial hindrance effect, which prevented adjacent carbon layers from coming closer. In order to identify the specific microstructure in HCs, the (002) peak was fitted into two spectral bands (Fig. S8), including a disordered band (~22.5°)

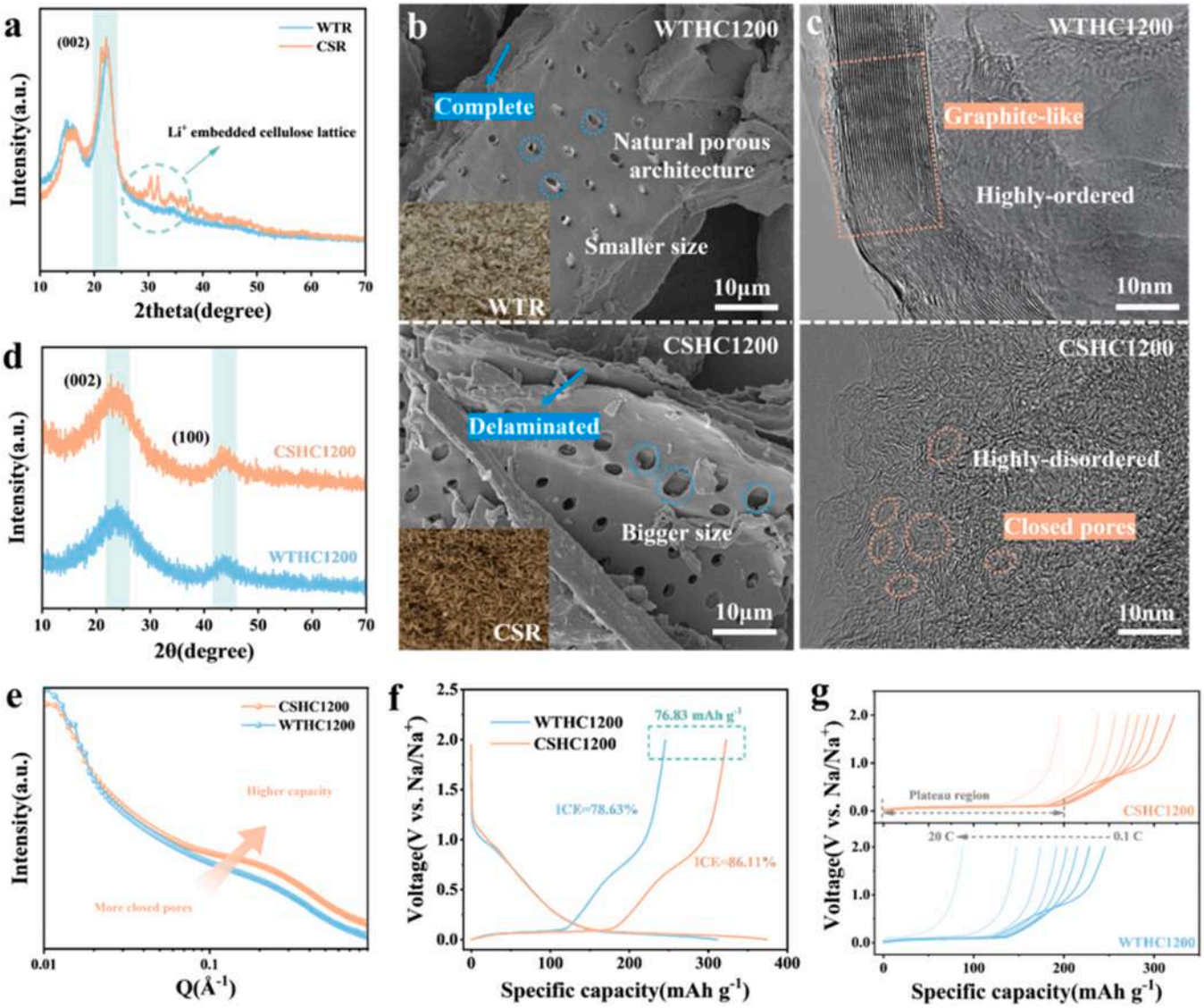


Fig. 3. Microstructure characterization of CSR, CSHC1200, WTR and WTHC1200. XRD patterns of (a) precursors (CSR and WTR) and (b) HCs samples (CSHC1200 and WTHC1200). (c) SEM images of CSHC1200 and WTHC1200 (insets show the optical photos of CSR and WTR), (d) TEM images and (e) SAXS analysis of CSHC1200 and WTHC1200. Electrochemical performance of CSHC1200 and WTHC1200. (f) initial GCD curves at 0.1 C (1 C=300 mA g^{-1}); (g) reversible capacity contributions from plateau region.

and a pseudo-graphitic band (~26.5°), characterized by aliphatic carbon atoms and aromatic carbon atoms, respectively [34]. The proportion of pseudo-graphite ribbons increased from 53.82% to 58.19%, indicating the promoting effect of swelling on the development of pseudo-graphite structure. In Raman spectra (Fig. S9), both samples exhibited two distinct broadened peaks near 1340 cm^{-1} (D-band) and 1590 cm^{-1} (G-band). The D-band is associated with sp^3 hybridized bonding in graphite-like regions, such as vibrations at carbon layer edges and defect sites, and G-band correspond to the in-plane stretching vibrations of sp^2 carbon atoms in aromatic rings or long chains, reflecting the vibrations of graphite crystallites. The degree of disorder in HCs is typically quantified by the area ratio of D- and G band (I_D/I_G), with higher values indicating greater disorder [35]. CSHC1200 exhibited a higher I_D/I_G value (Fig. S10 and Table S2) which is consistent with the deconvolution results of XRD. This can be attributed to the destruction of the ordered structure during the expansion process. Based on Brunauer-Emmett-Teller (BET) model, the specific surface area (SSA_{BET}) and porosity were analyzed using N_2 adsorption/desorption isotherms (Fig. S11). As shown in Fig. S11b, the pore sizes of both materials predominantly ranged between 1−10 nm, indicating the presence of micro-/meso-porous structures. CSHC1200 demonstrated a low SSA_{BET} of 12.09 $m^2 g^{-1}$ and a total pore volume (V_{total}) of 0.031 $cm^3 g^{-1}$, compared to 32.52 $m^2 g^{-1}$ and 0.071 $cm^3 g^{-1}$ for WTHC1200, respectively (Table S3). The reduced SSA_{BET} and V_{total} can be attributed to the removal of impurities, thereby optimizing the carbon layer rearrangement at high temperatures. The reduction of these two parameters is advantageous for reducing the formation of solid electrolyte interface (SEI) during the initial cycle. To characterize the closed-pores architecture inaccessible to N_2 physisorption, small-angle X-ray scattering (SAXS) was employed. CSHC1200 exhibited a more discernible platform at ~0.1 $Å^{-1}$ (Fig. 3e), indicating a larger concentration of closed pores which are the main sodium storage sites of HCs. This means that cellulose swelling is effective for the construction of closed pores, which is expected to deliver better performance in capacity. In addition, fitting with the Teubner-Strey model shows that the closed pore size of CSHC1200 is approximately 1.311 nm (Fig. S12), which is close to the optimal closed pore size reported in the current literature [36–39].

To validate this point, the electrochemical performance of

CSHC1200- and WTHC1200-based half-cells were evaluated at room temperature (25°C). As depicted in Fig. 3f, the galvanostatic charge/discharge (GCD) curves exhibited a plateau region (below 0.1 V vs. Na/Na^+) and a slope region (above 0.1 V vs. Na/Na^+). At the current density of 30 mA g^{-1} (0.1 C; 1 C=300 mA g^{-1}), the reversible specific capacities of CSHC1200 and WTHC1200 were 322.33 mAh g^{-1} and 245.50 mAh g^{-1}, respectively. Owing to the reduction of SSA_{BET}, CSHC1200 demonstrated a higher ICE of 86.11% compared to 78.63% of WTHC1200. Besides, CSHC1200 displayed remarkable rate capability, delivering reversible capacities of 322.33, 305.14, 293.69, 283.05, 272.01, 256.83, 238.52, 195.69 mAh g^{-1} at 0.1, 0.2, 0.5, 1, 2, 5, 10 and 20 C, respectively, significantly outperforming WTHC1200 and other reported HCs materials (Fig. S13 and Table S4) [40–49]. Obviously, the superior capacity retention of CSHC1200 at high current densities mainly comes from the plateau region (Fig. 3g), which is closely related to its higher closed-pore content and more stable SEI. When the rate was gradually restored to 0.1 C, CSHC1200 showed a high recovery rate of capacity (96.11%), which indicated its excellent stability across a wide range of current densities (Fig. S13). After analyzing the reversible capacity of different regions at various rates, we found that the difference in capacity of the two samples, generally shows an increasing trend in plateau region, while showing an opposite one in the other (Fig. S14). Surprisingly, the plateau region capacities of CSHC1200 and WTHC1200 exhibited a unique volcano-shaped curve, reaching a peak at 0.5 C. This is inconsistent with what has been reported in previous literature, where the capacity of plateau region generally decreases as the rate increases. An explanation of this part will be provided later. To further check the specificity of the swelling effect $Li[(H_2O)_n]^+$, we did control experiments using NaOH and KOH solutions under the same conditions (Fig. S15). The first cycle GCD curves show that the LiOH-treated (212.0 mAh g^{-1}) samples have higher plateau capacities than the NaOH- (NaOH-HC1200, 169.2 mAh g^{-1}) and KOH- (KOH-HC1200, 157.5 mAh g^{-1}) treated ones. This makes sense because Li^+ has the smallest bare ion radius but the largest hydrated size among alkali metal ions, so it can uniquely enter the crystalline regions of cellulose, causing intracrystalline swelling and forming closed pores. Na^+ and K^+ mainly just cause inter-crystalline swelling and can't form the closed pore structures needed for high plateau capacity.

2.3. Pyrolysis temperature optimization

To further optimize the microstructure of swelling HCs and investigate the synergistic effects between swelling treatment and carbonization temperature on closed pore characteristics, CSHC1000 and CSHC1400 were prepared by adjusting the carbonization temperature of CSR. All samples maintained natural porous architecture across different carbonization temperatures (Fig. S16). As shown in Fig. S17, the area of pseudo-graphitic band is positively correlated with carbonization temperature, which is highly consistent with the results presented in XRD patterns that, an increase in carbonization temperature led to a decrease in the interlayer spacing of carbon. Most of the impurity components also escaped through gasification in the mutual extrusion of the carbon layer, which is beneficial for reducing the disorder of microstructure. The decrease in I_D/I_G ratio confirmed this view (Fig. 4a and Fig. S18-19). The changes in microstructures can also be clearly observed in HR-TEM plots (Fig. 4b). The gradual sharpening of diffraction rings in the selected area electron diffraction (SAED) pattern usually indicates the growth of graphite microcrystal size. The planar features of the pseudo-graphitic carbon layers became more pronounced and approached each other under van der Waals forces, which caused a reduction in the spacing between carbon layers. During this process, the size of graphite crystallites increased, including the microcrystalline width L_a and stacking height L_c (Table S2). From the perspective of pore structure properties, the N_2 adsorption/desorption isotherms showed that CSHC1000 exhibited a typical Type I isotherm (Fig. S20a), with a sharp increase in adsorption at low pressures followed by a plateau, indicating the presence of abundant micropores. In contrast, CSHC1200 and CSHC1400 displayed Type IV isotherms with slight hysteresis loops, indicating a significant decrease in micropore content, which was confirmed by the pore size distribution in Fig. S20b. The sharp decrease in micropore content led to a drop of several orders of magnitude in SSA_{BET}. Compared with CSHC1000 (727.96 m^2 g^{-1}), SSA_{BET} of CSHC1200 (12.09 m^2 g^{-1}) or CSHC1400 (7.95 m^2 g^{-1}) is more consistent with the pore characteristics of HCs. Based on SAXS spectrum, we can find that the increase in carbonization temperature increased the closed porosity of samples (Fig. 4c). This is because the formation of closed pores mainly arose from the bending and sealing mechanisms of graphene carbon layers at high temperatures. The higher the temperature, the denser the carbon layers were arranged, and the originally connected open pores were also sealed in this process, forming more closed pores. A more detailed schematic diagram of the microscopic evolution of CSHCs is shown in Fig. 4d. Specifically, with the increase in carbonization temperature, the degree of graphitization, the size of graphite microcrystals, and the closed pore volume in CSHCs increase.

Previous studies have shown that OCFGs play a crucial role in the electrochemical behavior of HCs [50]. FT-IR analysis revealed that the change of pyrolysis temperature did not significantly alter the fundamental molecular bonding configurations or categories in CSHCs (Fig. S21). The XPS survey spectrum exhibited prominent peaks at 284.80 eV and 533.38 eV, indicating the presence of C and O elements (Fig. S22). Fortunately, no Li signal was detected, indicating that the surface Li^+ content is below the XPS detection limit, consistent with the removal of most Li^+-compounds during the high-temperature pyrolysis. As carbonization temperature elevated, the C/O atomic ratio progressively increased from 17.32% to 22.98% (Fig. S23 and Table S5), which is attributed to the breaking of the C–O polar bonds, causing oxygen-containing substances to vaporize and escape. The high-resolution C 1s spectral deconvolution resolved four components (Fig. S24), including C–C/C=C (~284.7 eV), C–O (~286.2 eV), O–C=O (~289.0 eV), and π–π* (~291.2 eV). In particular, the π–π* peak is indicative of the aromatic structure and originates from the lignin naturally present in ramie. This peak originated from the electron excitation in the photoemission process, where delocalized high-energy π electrons were excited to the anti-bonding π–π* orbitals, causing additional energy loss. Therefore, its energy is usually 4−6 eV higher than the binding energy of C–C/C=C peak [51]. With the carbonization temperature increasing, initially disordered aromatic ring structures merged into extended conjugated systems, leading to a positive correlation between the area of π–π* peak and carbonization temperature (Table S6). To further understand the impact of O atoms in OCFGs, high-resolution spectral deconvolution of O 1s was performed (Fig. 4e), revealing three peaks corresponding to C=O (~533.6 eV), –OH (~532.5 eV), and C–O (~531.3 eV). Notably, CSHC1200 exhibited the highest C=O proportion (Fig. S25 and Table S7), which is particularly significant because C=O is recognized as favorable sites for reversible Na^+ storage in HCs [43]. These results indicate that the swelling treatment and the pyrolysis temperature must be appropriately matched to maximize their synergistic effect. The swelling step creates the structural prerequisite for closed-pore formation, while the pyrolysis temperature governs the development of closed pores and the retention of C=O groups.

To deeply reveal this at the atomic scale, we simulated three carbon substrate models (Fig. S26) based on density functional theory (DFT): perfect graphene (G-perfect), defective graphene (G-defect), and carbonyl graphene (G-carbonyl). It is well known that at low potentials, the localized chemical environment on the HCs surface plays a key role in regulating the adsorption behavior of Na^+. Therefore, we evaluated the adsorption energy of Na on the three surface models (Fig. 4f). The results show that the adsorption energy (E_{ads}) of Na on the surface of G-perfect is 0.343 eV, indicating that adsorption is thermodynamically unfavorable. After introducing vacancy defects, the Ea_{ds} significantly decreased to –1.94 eV, indicating spontaneous adsorption. Further

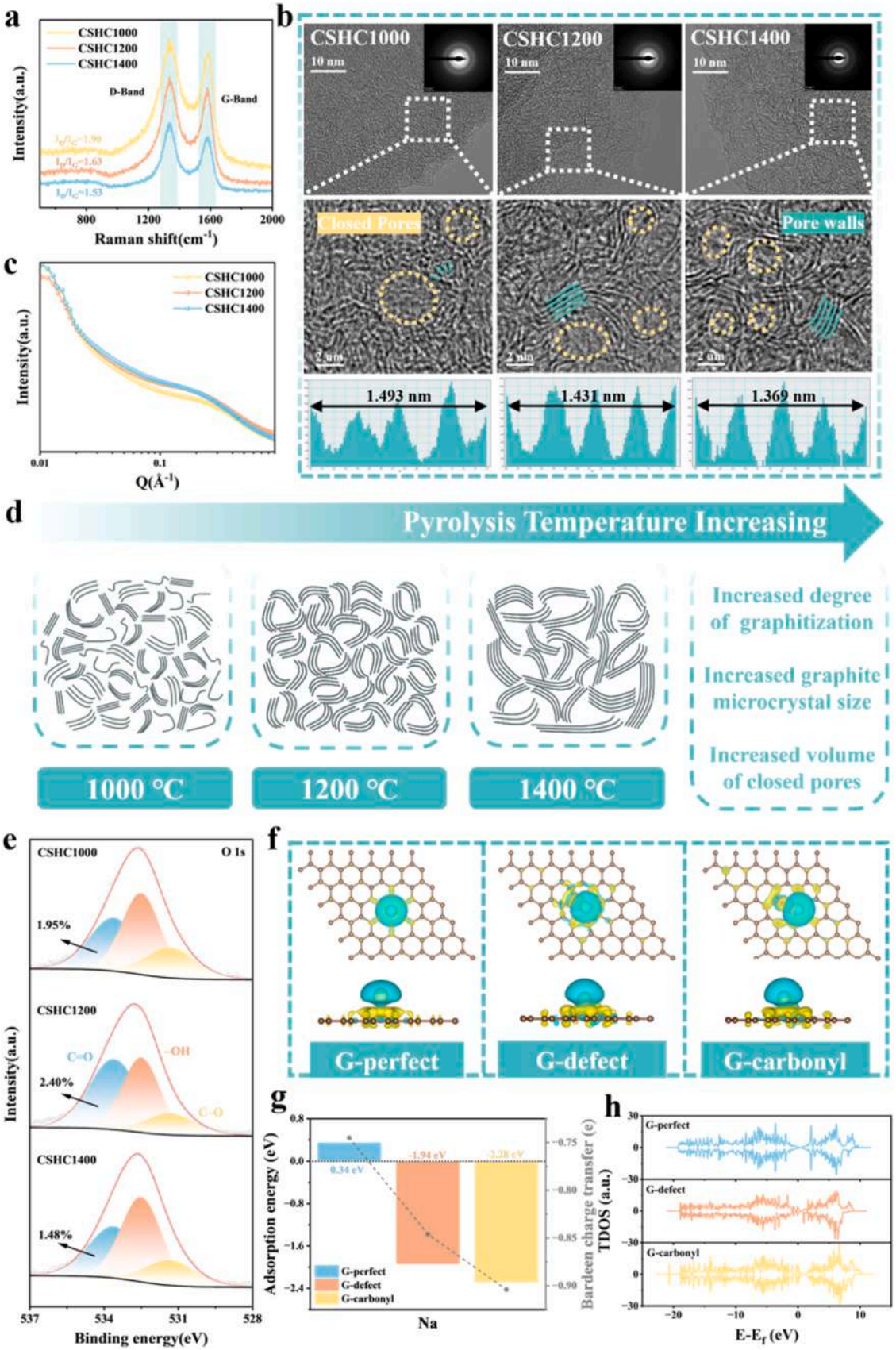


Fig. 4. Microstructure characterization of CSHCs prepared at different pyrolysis temperatures. (a) Raman spectra; (b) HR-TEM images (insets show the corresponding SAED patterns); and (c) SAXS analysis. (d) Schematic illustration of the effect of increased pyrolysis temperature on the evolution of the microstructure of CSHCs. (e) High-resolution O 1s spectra of CSHCs. Calculations of three carbon-based substrate models (G-perfect, G-defect and G-carbonyl) based on density

functional theory (DFT). (f) Differential charge density map of Na adsorption model, (g) adsorption energy (E_{ads}) and Bader charge transfer; and (h) density of states diagram.

incorporation of C=O showed that defect carbon decorated with O atoms exhibits the strongest adsorption affinity, with an Ea_{ds} as low as –2.28 eV. This indicates that the synergistic effect of structural defects and OCFGs can significantly enhance the thermodynamic interaction between the carbon substrate and Na. To further elucidate the electronic mechanism of this interaction, an in-depth analysis combining differential charge density and Bader charge was conducted. Compared with the weak charge variation at G-perfect interface, the G-carbonyl interface exhibited intense charge polarization and localized electron accumulation between Na and the more electronegative O atoms. Quantitatively, Na loses 0.745 e^-, 0.846 e^-, and 0.904 e^- when adsorbed on G-perfect, G-defect and G-carbonyl, respectively (Fig. 4g). The charge transfer amounts are highly consistent with the spatial distribution of charge, revealing that C=O acts as a strong nucleophilic site, promoting strong chemical bonding and directional electron transfer between Na^+ and the carbon substrate. Moreover, the calculation of the density of states validates the advantage of surface chemical state regulation from the intrinsic electronic structure level (Fig. 4h). At the Fermi level, the broadening of electronic state distribution in three systems follows the order of G-carbonyl > G-defect > G-perfect, which implies improved electronic conductivity, facilitating rapid interfacial charge transfer and enhanced electrochemical kinetics. These theoretical insights into electronic structure and adsorption behavior of carbon lay the foundation for correlating surface chemical characteristics with electrochemical performance.

2.4. Electrochemical performance of CSHCs

The distinct microstructural and compositional characteristics of CSHCs critically governed their electrochemical behavior. As shown in Fig. 5a, initial cycling revealed comparable first-cycle reversible capacities at 0.1 C for CSHC1200 (322.33 mAh g^{-1}) and CSHC1400

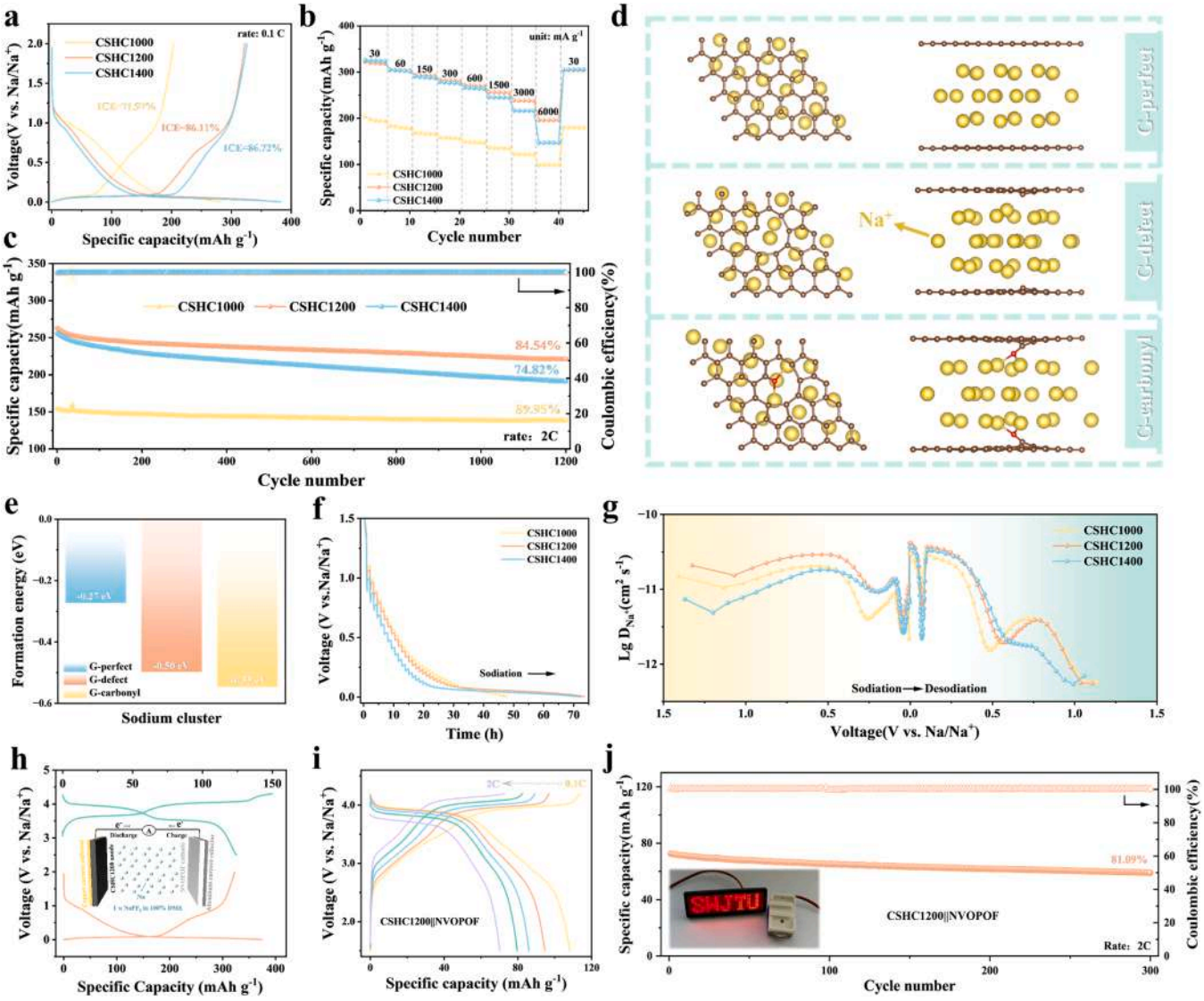


Fig. 5. Electrochemical performance of CSHCs based half-cells. a) Initial GCD curves at 0.1 C (1 C=300 mA g^{-1}), b) rate capability at 0.1−20 C, and c) cycling performance at 2 C. d) Double-layer parallel closed-pore model for simulating high-concentration Na pore-filling behavior. e) Formation energy (E_{form}) of 27-Na-atom sodium cluster. Electrochemical behavior of CSHCs. f) GITT profiles of discharge process, g) the calculated Na^+ diffusion coefficients during the charge/discharge processes. Electrochemical performance of CSHC1200||NVOPOF full-cell. h) Typical GCD curves of CSHC1200 and NVOPOF in half-cells respectively, i) rate capability at 0.1−2 C, and j) cycling performance at 2 C (insets show the LED light powered by the CSHC1200||NVOPOF full-cell).

(325.97 mAh g^{-1}), significantly exceeding CSHC1000 (203.28 mAh g^{-1}). The ICE of CSHCs exhibited marked temperature dependence (Table S8), that higher the carbonization temperature, the higher the ICE. This is originated from reduced open pore density and diminished surface defects at higher carbonization temperatures, which hindered irreversible Na^+ capture and excessive SEI formation during the first charge/discharge process. When it comes to rate performance, although the reversible capacity of CSHC1200 was slightly lower than that of CSHC1400 at 0.1 C, it achieved a comeback at 0.5 C, and the capacity gap between them gradually widened as the current density further increased (Fig. 5b). This is because Na^+ has ample time to migrate and intercalate at low current densities, so the total number of accessible active sodium storage sites determines its capacity. While with the kinetic pressure of the reaction increases at higher current densities, the diffusion rate of Na^+ within the bulk phase and at the interface becomes the main factor limiting performance. At this time, other active sites (e.g., defects) in HCs are needed to cooperate with closed pores to store Na^+, and the advantage of the closed pore content gradually diminishes. Notably, the characteristic volcano-shaped curve was further confirmed in the plateau capacity data of CSHC1000 and CSHC1400 (Fig. S27 and Table S9), necessitating a detailed mechanistic investigation in the subsequent section. Furthermore, we revealed the differences in the cycling stability of the samples at 2 C (Fig. 5c). We found that the increase in carbonization temperature led to a decline in cycling performance. Even if slightly inferior to CSHC1000 (89.95%), the capacity of CSHC1200 was only from 262.84 mAh g^{-1} dropped to 222.21 mAh g^{-1}, with a capacity retention rate of 84.54% after 1200 cycles. Based on the decent cycling performance of CSHC1200, further tests were carried out at 20 C. As shown in Fig. S28, after 10,000 cycles, CSHC1200 achieved an excellent capacity retention of 70.87%. To examine the origin of sodium storage capacity in plateau region, a double-layer parallel closed-pore model was constructed to simulate high-concentration Na^+ pore-filling behavior (Fig. 5d). Within the confined space accommodating 27 Na, the formation energy (E_{form}) of sodium clusters in G-perfect, G-defect, and G-carbonyl pore wall models are −0.273 eV, −0.498 eV and −0.547 eV, respectively (Fig. 5e). The lowest E_{form} of G-carbonyl confirms that the C=O groups on the pore walls stabilize sodium clusters thermodynamically within the confined pore space, while the closed pores themselves provide the necessary physical confinement for storing the clusters. This complementary synergy between physical confinement and chemical functionality supports the high plateau capacity of CSHC1200.

To elucidate the kinetic mechanisms and difference in Na^+ storage processes among CSHCs, we systematically employed GITT testing, cyclic voltammetry (CV), and electrochemical impedance spectroscopy (EIS). GITT test was carried out at 30 mA g^{-1} of pulse current for 10 minutes between the rest intervals for 1 hour to measure the diffusion coefficient of Na^+ (D_{Na^+}), which indicates the rate of Na^+ migration within HCs (Fig. 5f, Fig. S29 and Fig. S30a). All samples exhibited a similar shape and the order of magnitude of D_{Na^+} was in the range of 10^{-12}~10^{-10} (Fig. 5g and Fig. S30b). The D_{Na^+} of CSHC1200 was relatively higher, which is a direct reflection of the excellent diffusion rate. EIS investigated the electrode impedance characteristics of CSHCs. The Nyquist plots for all samples consisted of a high-frequency semicircle (R_{ct}) and a low-frequency straight line (Z_w). R_{ct} reflects the resistance of the charge across the SEI in the electrode reaction, and the larger the diameter, the greater the resistance. Z_w is related to the solid-phase diffusion of Na^+ in the HCs, and the larger the slope, the smaller the impedance. CSHC1200 showed the lowest R_{ct} and Z_w before and after cycling (Fig. S31). The optimized interfacial reaction kinetics was attributed to its appropriate defect concentration and closed-pore wall structure. Based on Arrhenius equations and R_{ct} obtained at different temperatures (20, 30, 40, 50 and 60°C), it is possible to calculate the activation energy (E_a) for Na^+ to cross the barrier, realize charge transfer and participate in the electrochemical reaction [52]. As expected, CSHC1200 has a smaller E_a than CSHC1400 (Fig. S32). Although CSHC1000 had the lowest E_a, but this was attributed to the highest defect concentration which will be ultimately harmful to electrochemical performance. Thus, CSHC1200 achieved an optimal balance between structural parameters and electrochemical performance from the perspective of EIS analysis. The CV analysis with a range of 0.001−2 V at different scan rates (0.1−0.8 mV s^{-1}) elucidated reaction dynamics. At 0.1 mV s^{-1}, CSHC1200 and CSHC1400 electrodes had a pair of sharp and symmetrical oxidation/reduction peaks around 0.1/0.01 V, corresponding to the extraction/insertion of Na^+ on the surface of the anodes (Fig. S33). Compared to CSHC1400, the enhanced current response of the CSHC1200 indicated a more active electrochemical reaction. Interestingly, the CSHC1000 electrode with the lowest reactivity featured two redox peaks, which may be related to more developed microporous structure, stimulating Na^+ deposition. According to relevant formula, the relationship between the response current and the square root of the scanning rate can be calculated [53]. Based on the linear regression of redox peaks yielded slope parameters b values (Fig. S34 and Fig. S35), the CV curves can be divided into surface-capacitive (b = 1) and diffusion-controlled (b = 0.5) processes. As shown in Fig. S35, CSHC1200 (b ≈ 0.68) exhibited electrode kinetics with a mix of diffusion and surface capacitance advantages, which is conducive to achieving both high capacity and high-rate performance, in contrast to the diffusion-controlled behavior of CSHC1400 (b ≈ 0.59) and surface-controlled CSHC1000 (b ≈ 0.89). Additionally, Fig. S36 depicted the capacitance contribution of CSHCs at different scan rates, which further revealed the structure-performance relationship. CSHC1000 has the highest defect concentration, showing an extremely high capacitance-controlled contribution. Due to the higher degree of graphitization and lower surface activity, CSHC1400 has a lower capacitance-controlled contribution. In contrast, while retaining enough closed pores for Na^+ storage, CSHC1200 has abundant surface active sites and excellent ion channels, giving it a stronger inherent fast charge storage capability. Therefore, CSHC1200 can dominate charge storage through efficient capacitive behavior at high rates, which is the key mechanism behind its outstanding rate performance. Collectively, these multiscale electrochemical analyses established that HCs architectures require balanced optimization of closed pore density, defect concentration and interlayer spacing. They govern the complex interplay between capacitive and diffusion-controlled processes essential for high-performance Na^+ storage.

To investigate the practical application potential of CSHC1200, we combined it with a layered oxides cathode $Na_3(VOPO_4)_2F$ (NVOPOF) to assemble into a full-cell CSHC1200||NVOPOF (Fig. 5h). The rate performance of CSHC1200||NVOPOF is shown in Fig. 5i. When the current density increased from 0.1, 0.2, 0.5 and 1 to 2 C, the specific capacities were 109.81, 94.70, 86.09, 79.70, and 70.18 mAh g^{-1}, respectively (based on the mass of the active cathode material). After 300 cycles at 2 C, the full-cell demonstrated a capacity retention rate of 81.09% (Fig. 5j). The energy density and power density were calculated based on the total mass of the active anode and cathode materials. At a high-power density of 20.19 W kg^{-1}, the full-cell achieved an energy density of 221.06 Wh kg^{-1}, indicating a high potential for practical application in SIBs.

2.5. Sodium storage mechanism

It was mentioned earlier that the plateau capacity of the samples exhibited the unique volcanic curve, which has a peak at around 0.5 C. This uncommon dynamic behavior can be interpreted at a microscopic level through differential capacity (dQ/dV) analysis. As shown in Fig. S37, the intensity of the ~0.06 V main peak (labeled P_a), which represents closed-pore sodium storage, is synchronized with the plateau capacity, showing a non-monotonic change that first strengthens and then decreases. Different from the behavior of the P_a peak, the ~0.7 V oxidation peak (labeled P_b), which is clearly present at low rates (0.1−0.2 C), monotonically decreases with increasing rates and is

significantly weakened after 0.5 C. We found that under low-rate testing, the GCD curves of all samples exhibit an inward concave feature valley near 0.7 V (where the absolute value of the slope decreases). Surprisingly, this voltage valley coincides remarkably with the potential of the P_b peak in the dQ/dV curves. We believe that the P_b peak originates from a slowly dynamic interfacial process, which may involve two contributions: (i) the escape of Na^+ from the high-energy defects or residual OCFGs on the surface of HCs, and (ii) slow electrolyte decomposition or SEI membrane reconstitution that continuously occurs during this potential interval. These processes have large reaction time constants and are therefore particularly significant at low rates close to equilibrium. The sharp contrast in the changes of P_a and P_b reveals the reasons for the change in the plateau capacity (Fig. 6a). At a low rate of 0.1 C, the charging time is long, allowing slow side reactions to fully proceed, but this process may degrade the interface or block channels, which in turn suppresses the main reaction in the plateau region, resulting in a plateau capacity that does not reach its maximum and an obvious side reaction P_b. As the rate increases to an optimal value (0.5 C), the charging time shortens. The side reactions are moderately suppressed, and their interference with the main reaction is reduced, allowing the main reaction to proceed efficiently, the plateau capacity to reach its peak, and the side reaction peak to weaken simultaneously. When the rate

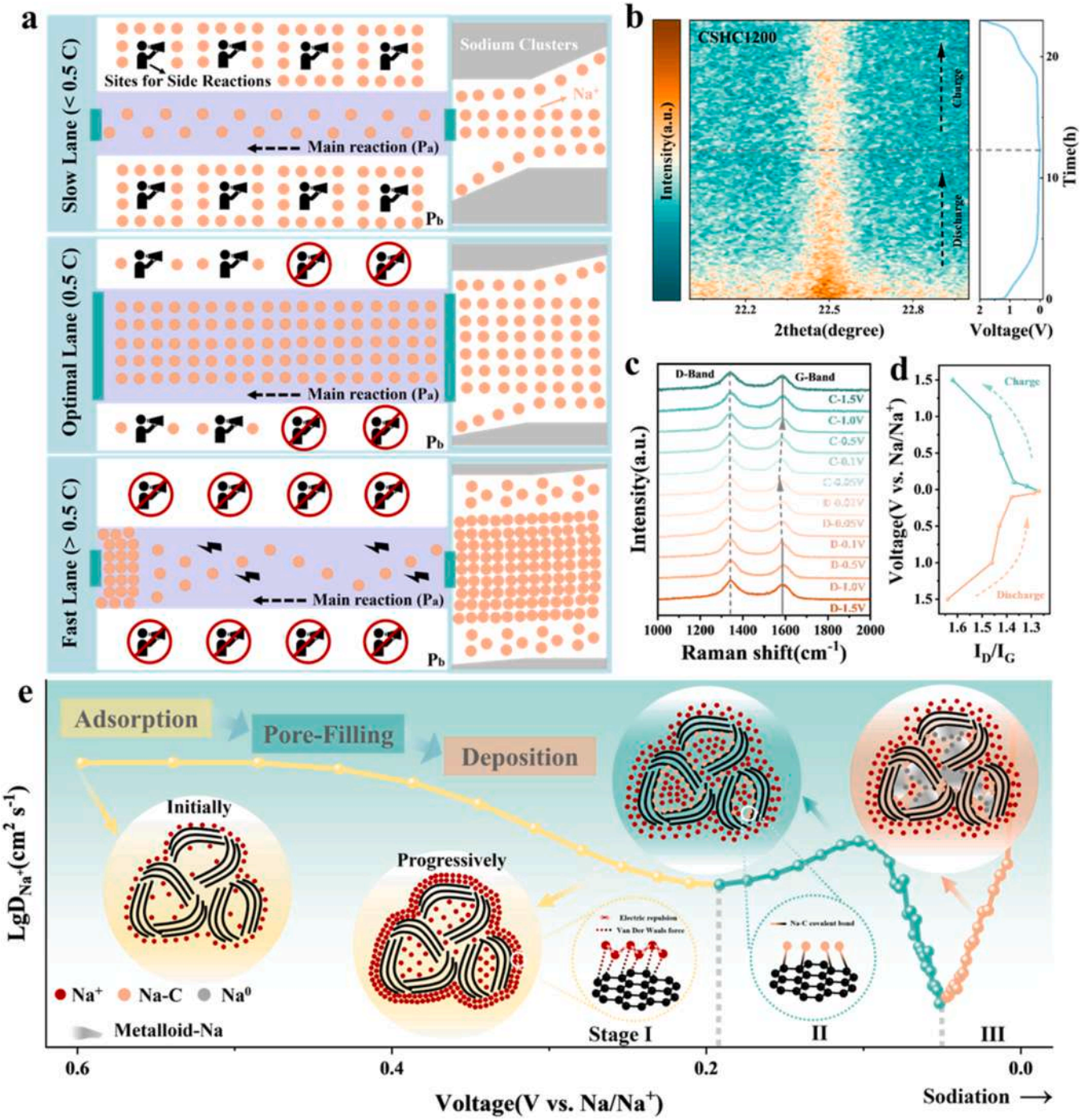


Fig. 6. (a) Schematic diagram of the evolution of platform region capacity dominated by the competition between main and side reactions at different rates. (b) In-situ XRD spectra, (c) ex-situ Raman spectra and (d) I_D/I_G value changes with the voltage of CSHC1200 electrodes during the charge/discharge process. (e) Schematic diagram of the sodium storage mechanism of CHSC1200.

continues to increase to a high level, the charging time becomes too short, and the main reaction is inherently limited by slow kinetics and cannot be completed, causing the plateau capacity to drop sharply. The entire process reflects the competitive relationship between side reactions and the main reaction, which changes inversely with the rate.

In order to verify the possible storage mechanism of Na^+ in HCs, electrochemical in-/ex-situ testing was performed on CSHC1200. In-situ XRD results were shown in Fig. 6b, the (002) diffraction peak position corresponding to HCs remained basically unchanged during the process of discharge and charge, indicating that the interlayer position of pseudo-graphitic carbon in CSHC1200 may not be used as a storage site for Na^+. Based on the adsorption-pore filling mechanism, sodium clusters may form in closed pores in the plateau region. The CSHC1200 half-cells were discharged to 0.1, 0.01, 0.001 and 0.0001 V (vs. Na/Na^+), respectively, and disassembled at open-circuit potential. The electrodes were then immersed in the 1% phenolphthalein ethanol solution. Fig. S38 showed the optical images of CSHC1200 electrodes discharged to different potentials. In the presence of sodium clusters, the phenolphthalein indicator solution gradually turned red. Notably, a gradual darkening of the phenolphthalein indicator was observed as the CSHC1200 electrodes were discharged to progressively lower potentials. This observation hints at a potential link between the plateau capacity and sodium clustering within closed pores. To gain further insight into the structural and bonding changes during cycling, we conducted ex-situ Raman spectroscopy. As shown in Fig. 6c, during the initial stage of sodium intercalation (1.5−0.5 V), the position of the G-band remains basically unchanged, indicating that the adsorption of Na^+ on the exposed surface has little impact on the carbon framework structure. As the depth of discharge increases (0.5−0.02 V), the G-band exhibits a significant redshift, corresponding to the formation of closed pores as Na^+ enters closed pores or stacked carbon layers, leading to changes in the local electronic structure. This phenomenon is related to electron-phonon coupling effect enhanced by electrons occupying the anti-bonding orbitals of the carbon framework, indicating a gradual charge transfer to the carbon matrix and the formation of strong Na−C interactions. Therefore, the abundant defects and nanoporous structure in CSHC1200 play a key role in promoting Na^+ adsorption, pore filling (Na−C interactions), and sodium cluster formation (Na−Na interactions). During desodiation, the G-band position shows a highly reversible trend, suggesting that the extraction of Na^+ from closed pores is structurally recoverable. In contrast, the D-band position remains stable throughout the cycling, meaning that the adsorption of Na^+ at defect sites has almost negligible effect on the defect structure. Moreover, the adsorption of Na^+ at active sites and the filling of closed pores slightly reduce the disorder of the carbon framework during sodiation, resulting in a decreased I_D/I_G ratio (Fig. 6d). After desodiation, the I_D/I_G ratio can recover close to its initial value, corresponding to the restoration of the highly disordered structure [52–54]. Based on the above analysis, the sodiation process can be basically divided into three distinct stages (Fig. 6e). Stage 1 (> 0.2 V): Initial rapid Na^+ adsorption at defect-dominated active sites in the transition zone led to surface charge accumulation, increasing interionic repulsion and subsequent D_{Na^+} reduction. Stage 2 (0.2−0.05 V): Partial Na^+ entering the graphene carbon layers or pores may gain electrons from the carbon structure and underwent reduction reaction, which to some extent weakened the repulsive force between Na^+, leading to a slow increase in D_{Na^+}. Stage 3 (< 0.05 V): The continuous accumulation of Na^+ in the transition zone intensified ion repulsion, causing a gradual decrease in D_{Na^+}. When the voltage reached the critical value of ~0.05 V, Na^+ quickly overcame the barrier and underwent the deposition of Na^+, allowing microscopic stress to be rapidly released. This led to a sharp increase in D_{Na^+}, reaching a peak near 0 V, followed by the desodiation stage. In conclusion, this section reveals the competitive dynamics of Na^+ storage and the closed-pore dominated mechanism in HCs, providing key insights for optimizing high-rate performance of SIBs.

3. Conclusion

In summary, we proposed an innovative cellulose swelling strategy to induce the formation of closed-pore structures in HCs, optimizing the microstructure and surface state under the synergistic regulation of carbonization temperature, achieving simultaneous improvements in sodium storage capacity and rate performance. The results indicated that during the swelling strategy process, strongly polar hydrated ions can effectively disrupt the ordered structure of the crystalline regions of cellulose, expanding the interlayer spacing of carbon while generating in-situ vacancy defects. MD simulations further confirmed two critical aspects: $Li[(H_2O)_n]^+$ penetrate the crystalline regions to induce intra-crystalline swelling, and the associated H_2O molecules remain trapped within the structure during low-temperature drying, subsequently generating steam vapor upon carbonization to create closed pores. This facilitated the formation of closed pores during subsequent carbonization and optimized the defect concentration, thereby increasing sodium storage sites and enhancing Na^+ diffusion kinetics. From the perspective of half-cells, the optimized CSHC1200 achieved a high reversible capacity of 322.33 mAh g^{-1} at a current density of 30 mA g^{-1}, with an ICE of 86.11%. Remarkably, it displayed outstanding rate performance (195.69 mAh g^{-1} at 6,000 mA g^{-1}, with a capacity retention of 60.06%) and stable cycling performance (84.54% retention after 1,200 cycles at 600 mA g^{-1}, and 70.87% retention after 10,000 cycles at 6,000 mA g^{-1}). In addition, the phenolphthalein color change experiment demonstrated the presence of sodium clusters. Electrochemical in-/ex-situ characterization coupled with GITT tests during the charge-discharge process revealed three stages of Na^+ diffusion and storage behavior in CSHC1200. The full-cell tests of CSHC1200||NVOPOF demonstrated its practical application value, achieving an energy density of 221.06 Wh kg^{-1} at a power density of 20.19 W kg^{-1}. It can be seen that this innovative closed pores inducing generation strategy is an effective means to enhance the sodium storage capacity and rate performance of HCs, greatly promoting the development of advanced biomass-derived HCs materials in commercial SIBs systems.

Notes

The authors declared no competing financial interest.

CRediT authorship contribution statement

Kai Gu: Writing – original draft, Investigation, Conceptualization. **Junan Feng:** Software, Methodology. **Taiping Zeng:** Investigation. **Jingye Wang:** Investigation. **Guilin Feng:** Investigation. **Wen Xi:** Investigation. **Yihan Wang:** Investigation. **Jiahao Chen:** Investigation. **Minjie Chen:** Investigation. **Feitian Ran:** Supervision, Funding acquisition. **Jifei Liu:** Supervision, Funding acquisition. **Chunliu Xu:** Writing – review & editing, Supervision, Funding acquisition. **Yao Xiao:** Writing – review & editing, Supervision, Funding acquisition. **Weiqing Yang:** Writing – review & editing, Supervision, Funding acquisition.

Declaration of competing interest

The authors declare that they have no known competing financial interests or personal relationships that could have appeared to influence the work reported in this paper.

Acknowledgements

This work was supported by National Natural Science Foundation of China (No. 52372228, No. 22309203), Wenzhou Key Scientific and Technological Innovation Research Project (Grant No. ZG2023053), the Science and Technology Department project of Sichuan Province of China (No. 2024ZYD0013, No. 2025ZNSFSC0364), China Postdoctoral Science Foundation (2024M752669, 2024M762671, 2025T180291),

the Fundamental Research Funds for the Central Universities (Grant No. 2682025CX003, 2682025CX145). the Joint Innovation Fund Project of Lanzhou Jiaotong University and Corresponding Supporting University (LH2025015) and Central Government Guidance Fund for Local Science and Technology Development (25ZYJC002). We thank Analysis and Testing Center of Southwest Jiaotong University for their assistance in materials characterization.

Supplementary materials

Supplementary material associated with this article can be found, in the online version, at doi:10.1016/j.ensm.2026.105551.

Data availability

Data will be made available on request.

References

[1] Y. Chu, J. Zhang, Y.B. Zhang, Q. Li, Y.R. Jia, X.M. Dong, J. Xiao, Y. Tao, Q.H. Yang, Reconfiguring hard carbons with emerging sodium-ion batteries: a perspective, Adv. Mater. 35 (2023) 2212186.
[2] Y. Gao, H. Zhang, J. Peng, L. Li, Y. Xiao, L. Li, Y. Liu, Y. Qiao, S.L. Chou, A 30-year overview of sodium-ion batteries, Carbon Energ. 6 (2024) e464.
[3] H.Y. Hu, M.W. Yang, D.C. Chen, N.H. Xu, J.Y. Li, Y.F. Zhu, Y.B. Wu, H.H. Dong, J. Y. Wang, C.J. Yao, Y.P. Yan, S.Q. Chen, N.N. Wang, W.K. Pang, Y. Sun, J.Z. Wang, Y. Xiao, Spatially selective substitution for structural stabilization of sodium layered oxide cathodes, Angew. Chem. Int. Ed. 65 (2026) 2519108.
[4] L. Wang, S.Q. Fang, H.C. Wang, Q.Q. Peng, Y.F. Liu, H.H. Dong, H. Yan, Y. Wang, S. L. Chou, B. Sun, Y. Xiao, S.Q. Chen, Flexible self-supporting organic cathode with interface engineering for high-performance and wide-temperature sodium-ion batteries, Carbon Energ. 6 (2024) e632.
[5] Y. Sun, X.L. Shi, Y.L. Yang, G.Q. Suo, L. Zhang, S.Y. Lu, Z.G. Chen, Biomass-derived carbon for high-performance batteries: from structure to properties, Adv. Funct. Mater. 32 (2022) 2201584.
[6] S.J. Jiang, Y.S. Xu, X.W. Sun, L. Chen, Y.N. Li, L. Li, F.F. Cao, Lignocellulolytic bacterial engineering for tailoring the microstructure of hard carbon as a sodium-ion battery anode with fast plateau kinetics, J. Am. Chem. Soc. 147 (2025) 8088–8092.
[7] C. Nita, B. Zhang, J. Dentzer, C.M. Ghimbeu, Hard carbon derived from coconut shells, walnut shells, and corn silk biomass waste exhibiting high capacity for Na-ion batteries, J. Energy Chem. 58 (2021) 207–218.
[8] W.F. Tian, L. Wang, K.F. Huo, X.M. He, Red phosphorus filled biomass carbon as high-capacity and long-life anode for sodium-ion batteries, J. Power Sources 430 (2019) 60–66.
[9] T.Y. Xu, X. Qiu, X. Zhang, Y.Y. Xia, Regulation of surface oxygen functional groups and pore structure of bamboo-derived hard carbon for enhanced sodium storage performance, Chem. Eng. J. 452 (2023) 139514.
[10] Y.L. Wang, Z.L. Yi, L.J. Xie, Y.X. Mao, W.J. Ji, Z.J. Liu, X.X. Wei, F.Y. Su, C. M. Chen, Releasing free radicals in precursor triggers the formation of closed pores in hard carbon for sodium-ion batteries, Adv. Mater. 36 (2024) 2401249.
[11] Z. Tang, R. Zhang, H.Y. Wang, S.Y. Zhou, Z.Y. Pan, Y.C. Huang, D. Sun, Y.G. Tang, X.B. Ji, K. Amine, M.H. Shao, Revealing the closed pore formation of waste wood-derived hard carbon for advanced sodium-ion battery, Nat. Commun. 14 (2023) 6024.
[12] Z.H. Fu, D. Jiang, Z. Tang, Z. Tang, J. Zhou, R. Liu, H.H. Li, D. Sun, Y.G. Tang, H. Y. Wang, Revealing the blocking effect of hemicellulose on the formation of closed pores in reed-derived hard carbon for sodium-ion batteries, Chem. Eng. J. 505 (2025) 159431.
[13] X.H. Lei, L. Zhang, X.Y. Guo, Q.H. Tian, Y. Yang, Y. Yi, J. Shi, J.Y. Zhong, X.X. Cao, F.X. Wu, X.W. Wang, S. Wang, Sustainable biomass-derived hard carbon anode materials toward long-life sodium-ion batteries via the fractal regulation strategy, Sustain. Mater. Technol. 46 (2025) e01779.
[14] Z. Zheng, S.J. Hu, W.J. Yin, J. Peng, R. Wang, J. Jin, B.B. He, Y.S. Gong, H. W. Wang, H.J. Fan, CO2-etching creates abundant closed pores in hard carbon for high-plateau-capacity sodium storage, Adv. Energy Mater. 14 (2024) 2303064.
[15] Y.X. Huang, Z.D. Hou, J.F. Wang, Y.L. Li, T. Ma, D. Nan, C.G. Wei, J.G. Wang, Reconfiguring terminal species of bituminous coal to steer hard carbon toward high-capacity and fast sodium storage, Angew. Chem. Int. Ed. 64 (2025) e202423864.
[16] Z.Z. Wen, R.G. Zhao, T.T. Tian, T. Zhang, X. Wang, X.Y. Yang, W.Q. Song, Y. N. Chen, J. Ding, W.B. Hu, Molecular stitching in polysaccharide precursor for fabricating hard carbon with ultra-high plateau capacity of sodium storage, Adv. Mater. 37 (2025) 2420251.
[17] Q. Wang, Y.X. Qu, Y.X. Yuan, Z.Y. Chen, G.L. Feng, P.P. Dong, X.X. Jiao, Y.L. Zou, W.Q. Yang, 3D Molecular-reconstructed disordered precursor toward highly stable porous ramie carbon, Adv. Mater. 37 (2025) 2418997.
[18] Q. Wang, Y.X. Qu, J. Bai, Z.Y. Chen, Q.T. Luo, H.J. Li, J. Li, W.Q. Yang, High-yield ramie derived carbon toward high-performance supercapacitors, Nano Energ. 120 (2024) 109147.
[19] Z.Y. Chen, Y.Y. Chen, Q. Wang, T. Yang, Q.T. Luo, K. Gu, W.Q. Yang, Molecularly-regulating oxygen-containing functional groups of ramie activated carbon for high-performance supercapacitors, J. Colloid Interf. Sci. 665 (2024) 772–779.
[20] Q. Wang, Z.Y. Chen, Q.T. Luo, H.J. Li, J. Li, W.Q. Yang, Capillary evaporation on high-dense conductive ramie carbon for assisting highly volumetric-performance supercapacitors, Small 19 (2023) 2303349.
[21] Q. Wang, F.Y. Liu, Z.Y. Jin, X.R. Qiao, H.C. Huang, X. Chu, D. Xiong, H.T. Zhang, Y. Liu, W.Q. Yang, Hierarchically divacancy defect building dual-activated porous carbon fibers for high-performance energy-storage devices, Adv. Funct. Mater. 30 (2020) 2002580.
[22] Y.Y. Chen, Q. Wang, N.J. Chen, Q.T. Luo, H.J. Li, J. Li, W.Q. Yang, Internally-externally molecules-scissored ramie carbon for high performance electric double layer supercapacitors, Electrochim. Acta 439 (2023) 141583.
[23] Q. Wang, Y.Y. Chen, X. Jiang, N.A.X. Qiao, Y.H. Wang, H.B. Zhao, B. Pu, W. Q. Yang, Self-assembly defect-regulating superstructured carbon, Energ. Storage Mater. 48 (2022) 164–171.
[24] G.L. Zhang, H. Gao, D.Y. Zhang, J. Xiao, L.M. Sun, J.Y. Li, C.C. Li, Y.W. Sun, X. Y. Yuan, P. Huang, Y. Xu, X. Guo, Y.F. Zhao, Y. Wang, Y. Xiao, G.X. Wang, H. Liu, Transformative catalytic carbon conversion enabling superior graphitization and nanopore engineering in hard carbon anodes for sodium-ion batteries, Carbon Energ. 7 (2025) e713.
[25] Y.J. Xu, Y.Y. Wang, Z.Y. Gu, C.S. Zhao, X.L. Wu, S.R.P. Silva, B.H. Hou, Cellulose-grafting boosted pyrolysis nucleation: Achieving low-temperature construction of hard carbon anodes with long low-voltage plateau and ultrafast Na storage kinetics, Energ. Storage Mater. 75 (2025) 104031.
[26] Z.X. Lu, J. Wang, W.L. Feng, X.P. Yin, X.C. Feng, S.Y. Zhao, C.X. Li, R.X. Wang, Q. A. Huang, Y.F. Zhao, Zinc single-atom-regulated hard carbons for high-rate and low-temperature sodium-ion batteries, Adv. Mater. 35 (2023) 2211461.
[27] H. Li, M.H. Zhao, Y. Wu, X.M. Yang, Z.H. Yang, L. Chen, J.T. Zhao, W.T. Zhang, J. L. Li, Step-temperature strategy enables closed-pores in hard carbon achieving high plateau capacity for sodium ion storage, Carbon 244 (2025) 120641.
[28] H.L. Sun, Z.H. Li, F. Yuan, J.H. Peng, Z.J. Li, Q.J. Sun, Q.J. Wang, D. Zhang, W. Wang, B. Wang, Hydrogen bond chemically mediated closed pore in hard carbon extending low-voltage plateau capacity for sodium storage, Chem. Eng. J. 505 (2025) 159452.
[29] J.D. Wang, T. Qiu, J. Xie, F. Liu, J.F. Wu, A.L. Li, J. Wang, J.P. Cheng, CO2 activation-induced closed pores in hard carbon derived from bamboo for enhanced sodium-ion storage, J. Colloid Interf. Sci. 703 (2026) 139177.
[30] A. Kamiyama, K. Kubota, D. Igarashi, Y. Youn, Y. Tateyama, H. Ando, K. Gotoh, S. Komaba, MgO-template synthesis of extremely high capacity hard carbon for Na-ion battery, Angew. Chem. Int. Ed. 60 (2021) 5114–5120.
[31] J. Mao, H. Abushammala, L.B. Pereira, M.P. Laborie, Swelling and hydrolysis kinetics of Kraft pulp fibers in aqueous 1-butyl-3-methylimidazolium hydrogen sulfate solutions, Carbohydr. Polym. 153 (2016) 284–291.
[32] J.P. Peng, Y.H. Huang, R.W. Fu, J.Q. Lu, W.Q. Wang, W.T. Zhu, Y.X. Yu, F. Guo, H. Y. Mai, Microscopic dissolution process of cellulose in alkaline aqueous solvents and its application in CNFs extraction- investigating temperature as a variable, Carbohydr. Polym. 322 (2023) 121361.
[33] W.S. Zhang, S. Okubayashi, T. Bechtold, Fibrillation tendency of cellulosic fibers. Part 1: effects of swelling, Cellulose 12 (2005) 267–273.
[34] Z.D. Hou, M.W. Jiang, D. Lei, X. Zhang, Y.Y. Gao, J.G. Wang, Regulation of pseudographitic carbon domain to boost sodium energy storage, Nano Res. 17 (2024) 5188–5196.
[35] K. Gu, Z.Y. Chen, Y.X. Yuan, T. Yang, Y.H. Wang, L. Zhou, L.C. Wu, G.L. Feng, W. Q. Yang, Difluorocarbene grafted on carbon for high-power supercapacitors, J. Energy Chem. 118 (2026) 591–601.
[36] Z.X. Yu, X. Li, N. Sun, H. Chen, R.A. Soomro, B. Xu, Synergistic regulation of closed pore architecture and interface engineering in hard carbon for high energy density sodium-ion batteries, Energ. Storage Mater. 82 (2025) 104612.
[37] Y.X. Wang, W. Zhang, N. Sun, R.A. Soomro, G.P. Xu, B. Xu, Confined carbonization of pitch assists the closed pore engineering of coal-based carbon for superior Na-ion storage, ACS Appl. Mater. Interf. 17 (2025) 15436–15445.
[38] R. Kong, N. Sun, Z.X. Yu, S.J. Zhou, X. Li, R.A. Soomro, B. Xu, Polydopamine-assisted synergistic regulation of surface chemistry and pore architecture in petroleum coke-derived carbons for high-power sodium-ion batteries, Adv. Funct. Mater. 36 (2026) 74902.
[39] X. Li, N. Sun, S.H. Zhang, R.A. Soomro, B. Xu, Closed pore structure engineering from ultra-micropores with the assistance of polypropylene for boosted sodium ion storage, J. Mater. Chem. A 12 (2024) 12015–12025.
[40] Z. Tang, R. Liu, D. Jiang, S.Q. Cai, H.H. Li, D. Sun, Y.G. Tang, H.Y. Wang, Regulating the pore structure of biomass-derived hard carbon for an advanced sodium-ion battery, ACS Appl. Mater. Interf. 16 (2024) 47504–47512.
[41] X.H. Lei, L. Zhang, X.Y. Guo, Q.H. Tian, X.M. Fan, H. Tong, Y. Yang, Regulation of composition, microstructure, and pore structure of biomass-based hard carbon to boost the sodium storage performance, J. Energ. Storage. 101 (2024) 113792.
[42] Z.Y. Huang, J.H. Huang, L. Zhong, W.L. Zhang, X.Q. Qiu, Deconstruction engineering of lignocellulose toward high-plateau-capacity hard carbon anodes for sodium-ion batteries, Small 20 (2024) 2405632.
[43] G.L. Feng, X. Yang, X.H. Liu, Y.B. Wang, Y.T. Xie, P.P. Dong, X.X. Jiao, C.L. Xu, J. M. Zhao, Y.S. Hu, W.Q. Yang, Microbially glycolysis-regulated hard carbons for sodium-ion batteries, Nano Energ. 136 (2025) 110728.
[44] S.Y. Zhou, Z. Tang, G.H. Jin, J.J. Tu, A.S. Dhmees, Y.G. Tang, D. Sun, R. Zhang, H. Y. Wang, Understanding the relationship of closed pore structure in biomass-derived hard carbon with cellulose regulating strategy, Small 20 (2024) 2407341.

[45] Y.X. Zhang, Z.R. Zhou, Q.Y. Lin, Q.X. Zhang, L.S. Fan, Precise decoupling of biomass components to engineer hard carbon microcrystalline architecture for enhanced sodium-ion storage performance, Small 21 (2025) e07313.
[46] Y.X. Zhang, Z.R. Zhou, Q.Y. Lin, Q.H. Jing, Z.J. Wang, S.Q. Yan, J. Guo, Y. Shuai, L. S. Fan, Open sesame: tailoring the microstructure of biomass-derived hard carbon for high-efficiency sodium-ion battery anodes, Chem. Eng. J. 515 (2025) 163768.
[47] L.Y. Gao, W.J. Zeng, G.Z. Liu, H.B. He, Multi-scale optimization of betel nut shell-derived hard carbon: hierarchical porous structure, local graphitization modulation, and binder design for ultrafast sodium storage, Chem. Eng. J. 517 (2025) 164381.
[48] Y.F. Shen, B.J. Fan, Y.H. Xin, Q.B. Zhou, Y.S. Wang, H. Zhou, K.Y. Zhao, F. Wu, H. C. Gao, Ternary deep eutectic solvent-Mediated rapid extraction of highly crystalline cellulose enabling closed-Pore regeneration of hard carbon anode for ultrafast sodium storage, Carbon 243 (2025) 120594.
[49] C.H. Yu, Y.H. Guan, P. Huang, J.Q. Wang, Y. Wang, J.M. Sun, W. Ai, Crosslinked starch-derived hard carbon with abundant closed pores for enhanced plateau capacity in sodium-ion storage, Carbon 247 (2026) 121020.
[50] Y.F. He, D. Liu, Q.Y. Li, Z.Y. Zhu, R.B. Wu, Advances in oxygen-containing functional groups-modified hard carbon anodes for sodium-ion batteries, Mater. Sci. Eng. R Rep. 168 (2026) 101143.
[51] L.B. Wang, Z.K. Xu, P. Lin, Y. Zhong, X.L. Wang, Y.F. Yuan, J.P. Tu, Oxygen-crosslinker effect on the electrochemical characteristics of asphalt-based hard carbon anodes for sodium-ion batteries, Adv. Energy Mater. 15 (2025) 2403084.
[52] N. Lan, Y.S. Shen, J.Y. Li, H.N. He, C.H. Zhang, Cell-shearing chemistry directed closed-pore regeneration in biomass-derived hard carbons for ultrafast sodium storage, Adv. Mater. 37 (2025) 2412989.
[53] Y. Liu, J. Yin, R.Y. Wu, H. Zhang, R. Zhang, R.Q. Huo, J.X. Zhao, K.Y. Zhang, J. Yin, X.L. Wu, H. Zhu, Molecular engineering of pore structure/interfacial functional groups toward hard carbon anode in sodium-ion batteries, Energ. Storage Mater. 75 (2025) 104008.
[54] W.N. Li, J.F. Li, B.W. Biney, Y.C. Yan, X.P. Lu, H. Li, H. Liu, W. Xia, D. Liu, K. Chen, A.J. Guo, Innovative synthesis and sodium storage enhancement of closed-pore hard carbon for sodium-ion batteries, Energ. Storage Mater. 74 (2025) 103867.